International Journal of Nanomedicine

Dovepress
open access to scientific and medical research

Open Access Full Text Article

ORIGINAL RESEARCH

DTPAA-Gd Functionalized Ultrasmall Au_{15}NCs Nanohybrids for Multimodal Imaging

This article was published in the following Dove Press journal:
International Journal of Nanomedicine

Minghao Wu[1,*]
Yanyan Zhang[1,2,*]
Na Zhuo[3]
Mingjie Wu[4]
Zhaoxiang Ye[1]
Xuening Zhang[2]

[1]Department of Radiology, Tianjin Medical University Cancer Institute and Hospital, National Clinical Research Center for Cancer, Tianjin's Clinical Research Center for Cancer, Key Laboratory of Cancer Prevention and Therapy, Tianjin 300060, People's Republic of China; [2]Department of Radiology, Second Hospital of Tianjin Medical University, Tianjin 300211, People's Republic of China; [3]Department of Ultrasound, Second Hospital of Tianjin Medical University, Tianjin 300211, People's Republic of China; [4]Institut National De La Recherche Scientifique-Energie Materiaux Et Telecommunications, Varennes,Quebec J3X 1S2, Canada

*These authors contributed equally to this work

Introduction: Multimodal imaging agent has the potential to overcome the shortage and incorporate the advantages of different imaging tools for extremely sensitive diagnosis. To achieve multimodal imaging, combining multiple contrast agents into a special nanostructure has become a main strategy; However, the combination of all of these functions into one nanoplatform usually requires a complicated synthetic procedure that results in heterogeneous nanostructure.

Methods: In this study, we develop ultrasmall gold nanoclusters with 15 gold atoms (Au_{15} NCs) functionalized with diethylenetriamine-pentaacetic acid dianhydride (DTPAA-Gd) as an optimized multimodal imaging agent to enhance imaging ability.

Results: The Au_{15}NCs-DTPAA-Gd nanohybrids possess the ultra-small size and are capable of enhancing the contrast in near-infrared fluorescence (NIRF), magnetic resonance (MR) and X-ray computed tomography (CT) imaging. Meanwhile, the integrated DTPAA-Gd component not only endow the nanohybrids to produce higher T_1 relaxivity ($r_1 = 21.4\ mM^{-1}\ s^{-1}$) than Omnipaque ($r_1 = 3.973\ mM^{-1}s^{-1}$) but also further enhance X-ray attenuation property of Au_{15}NCs. Importantly, the fluorescence intensity of Au_{15}NCs-DTPAA-Gd did not decrease compared with Au_{15}NCs. Ultimately, in vivo imaging experiments have demonstrated that Au_{15}NCs-DTPAA-Gd nanohybrids can be quickly eliminated from the body through the urinary system and has great potential for anatomical imaging.

Conclusion: These data manifest Au_{15}NCs-DTPAA-Gd present great potential as a multimodal contrast agent for disease diagnosis, especially for early accurate detection of tumors.

Keywords: multimodal imaging, ultrasmall gold nanoclusters, magnetic resonance imaging, near-infrared fluorescence, X-ray computed tomography

Introduction

Multimodal imaging nanoplatforms have evoked considerable interest to circumvent the limitations of single imaging modes and incorporate the advantages of different imaging modality.[1,2] A number of imaging techniques are introduced to these platforms for clinical diagnosis.[3,4] Among the diverse diagnostic techniques, X-ray computed tomography (CT) displays a high degree of spatial resolution of the hard tissues, and magnetic resonance imaging (MRI) is a powerful noninvasive modality with excellent soft-tissues resolution.[5,6] MRI and CT are suitable for anatomical reconstruction but have poor sensitivity and lack of molecular details.[7,8] Near-infrared fluorescence (NIRF) imaging is suitable for multiscale imaging from the cellular level to whole-body animals.[8,9] To achieve multifunction with MR, CT, and NIRF imaging, combining different imaging contrast agents into a macromolecule or encapsulation of them into a special nanostructure (e.g., hollow nanosphere or mesoporous nanoparticle) has become a main strategy.[10–13] However, the magnetic, X-ray attenuation, and fluorescent properties

Correspondence: Zhaoxiang Ye; Xuening Zhang
Email yezhaoxiang@163.com; luckyxn@126.com

submit your manuscript | www.dovepress.com
DovePress
http://doi.org/10.2147/IJN.S227169

usually originate from different molecules (or moieties),[13] and the combination of all of these functions into one nanoplatform usually not only requires a complicated synthetic procedure but lead to heterogeneous nanostructure.[14] Moreover, the introduction of an additional function is often accompanied by a decrease in the original function.[14] Therefore, it is necessary to explore effective synthetic strategies to fabricate excellent multifunction nanomaterials for multimodal bioimaging.

Gold nanoclusters (AuNCs) are intensely investigated as imaging contrast agents, owing to intensive fluorescence, extraordinary photostability, easy synthesis, and excellent biocompatibility.[15–18] Based on strong quantum confinement effect (SQCE) related to the size of clusters, AuNCs with different sizes may exhibit unique optical properties which extend from the red-spectral region to the biologically important near-infrared (NIR) window.[19,20] Recently, the composite nanomaterials with AuNCs have been extensively explored in multimodal imaging systems, such as fluorescence/CT, fluorescence/Magnetic resonance imaging (MRI), fluorescence/positron emission tomography (PET).[21,22] However, complicated synthetic procedure and interactions between different imaging components lead to the decrease and instability of the fluorescence characteristics of AuNCs. Fortunately, gold atoms with high atomic number and electron density possess high X-ray attenuation coefficient.[23,24] In our previous study, a sub-nanometer ultrasmall AuNCs with 15 gold atoms (Au_{15}NCs) may have access to both alluring optical characteristics and remarkable X-ray attenuation properties.[25] Therefore, Au_{15}NCs have great potential to be used as multimodal imaging platform to achieve both NIRF and CT imaging ability.

In this study, a novel kind of biocompatible and high-performing trimodal contrast agent (Au_{15}NCs-DTPAA-Gd) has been elaborately designed through covalently conjugating gadolinium-Diethylenetriamine-pentaacetic acid dianhydride (DTPAA-Gd) to Au_{15}NCs. Only by coupling Au_{15}NCs with gadolinium chelate, the obtained Au_{15}NCs-DTPAA-Gd exhibit dramatically promoted longitudinal relaxivity, near-infrared fluorescence signal and X-ray attenuation properties. It is worth noting that imaging components promote each other, which addresses the limitations of interference between imaging elements of conventional multimodal platforms. The in vivo imaging ability was validated on mice through MR and CT imaging, where Au_{15}NCs-DTPAA-Gd produced robust and prolonged contrast enhancement. The in vivo fluorescent imaging was validated on nude mice, where the red light produced by Au_{15}NCs-DTPAA-Gd under 485 nm excitation light can effectively penetrate the tissue and be observed by the human eye. The pharmacokinetics and biodistribution studies display appropriately decelerated plasma decay and renal excretion, which would be of great significance in accurate clinical diagnosis. The nanometer platform enables the perfect integration of each component and maximizes the imaging capacity of each component, which has great potential for medical imaging. To the best of our knowledge, this is the first report associated with the synthesis of DTPAA-Gd-functionalized Au_{15}NCs for NIRF/CT/MR trimodal imaging applications.

Materials and Methods

Materials

All chemicals of analytical grade were used without further purification. Chloroauric acid ($HAuCl_4 \cdot 4H_2O$) was purchased from Chemart (Tianjin, China). Reduced glutathione (rGSH, 98%) was obtained from Solarbio (Beijing, China). Diethylenetriamine-pentaacetic acid dianhydride (DTPAA, 95%) was purchased from Alfa Aesar (Shanghai, China). Gadolinium (Ⅲ) chloride ($GdCl_3 \cdot 6H_2O$), Dimethyl sulfoxide (DMSO, >99%), and Sodium acetate anhydrous (CH_3COONa) were purchased from Sigma-Aldrich (St. Louis, USA). 3-(4,5-Dimethylthiazol-2-yl)-2,5-diphenyltetrazolium bromide (MTT) was purchased from Merck (Germany). The other chemicals were purchased from Sigma-Aldrich (St. Louis, USA). Deionized water used throughout the experiments was acquired from Mili-Q water purification system after its resistivity reached 18.2 MΩ CM.

Human renal epithelial cell line (293T cell line) and human hepatocellular carcinoma cell line (HepG2 cell line) were acquired from Molecular Imaging Lab of Tianjin Medical University (Tianjin, China). The use of these cell lines had Molecular Imaging Lab of Tianjin Medical University review board approval. The female BALB/c mice and BALB/c athymic nude mice were obtained from Beijing Vital River Laboratory Animal Technology Co., Ltd (Beijing, China).

Synthesis of Au_{15}NCs-DTPAA-Gd

First, ultrasmall gold nanoclusters with 15 gold atoms (Au_{15}NCs) were prepared according to our previous report.[25] The freshly prepared aqueous solutions of $HAuCl_4$ (24 mM, 4.2 mL) were mixed into a 50-mL glass flask containing 43.5 mL of deionized water, and then 12 mg rGSH was added into $HAuCl_4$ solutions (rGSH/Au^{3+} 2:1) under vigorously stirring in water bath until a colorless and transparent

solution was formed. Subsequently, PH value of the above solution was adjusted to 9 with 1 M NaOH solution. Then, the above solution was heated to 70°C and kept gently stirring for 24 h. After reaction finished, the resultant Au_{15} NCs@GSH were precipitated by ethanol via centrifugation, washed several cycles and finally re-dispersed in PBS for next modification.

Then, the synthesis of Au_{15}NCs-DTPAA-Gd followed a typical amide reaction pattern with a slight modification. Firstly 24 mg of DTPAA dissolved in DMSO was added into 600 μL of the above-prepared Au_{15} NCs@GSH solution under gently stirred, and NaOH solution was used to adjust the pH to 8.5. After 2 h of stirring, 12 mg of $GdCl_3 \cdot 6H_2O$ dissolved in CH_3COONa (0.1M, 125 μL) was added dropwise into the above mixture under gently stirring, and the pH was regulated to 7 using 1 M $NaHCO_3$ solution. After stirring at 25°C for 24 h, the obtained Au_{15}NCs-DTPAA-Gd were washed with PBS by ultrafiltration centrifugation several times to extract excess Gd^{3+}. The final products were redispersed in 250 μL PBS and stored at 4°C for further use.

Characterization

Transmission Electron Microscopy (TEM) and Energy-dispersive X-ray Spectroscopy (EDX) element mapping were obtained using Jeol's Jem-2100F operating at 200 kV. Hydrodynamic size of nanohybrids dispersed in water was recorded by a Malvern Zeta Sizer 3000 HS (Malvern, UK). The surface potential charge was determined with the same instrument equipped with an AQ-827 electrode. The fluorescence spectra were characterized by 960PC spectrofluorometer (INESA, Shanghai, China). The absorption spectra were measured UV-visible-NIR UV1800 spectrophotometry (SHIMADZU, Suzhou, China). The fluorescence quantum yield of Au_{15}NCs and Au_{15}NCs-DTPAA-Gd was determined by relative measurement with rhodamine B as fluorescence standard. The quantities of Au and Gd in the Au_{15}NCs-DTPAA-Gd nanohybrids were determined by Inductively Coupled Plasma-Atomic Emission Mass Spectrometry (ICP-AES) analysis (Optima 5300 DV, Perkin Elmer, MA).

In vitro CT/NIRF/MR Imaging

The in vitro CT imaging of Au_{15}NCs, Au_{15}NCs-DTPAA-Gd and Omnipaque was acquired using Light Speed VCT system (General Electric Company, America) with imaging parameters: 120 keV, 80 mA, and a slice thickness of 0.625 mm. Evaluation of the X-ray attenuation intensity was carried out by loading the digital CT images in a standard display program (GE Advantage Workstation AW4.4) and then selecting a uniform round region of interest on the resulting CT image of each sample. Contrast enhancement (Hounsfield units, HU) was determined for each concentration of Au_{15}NCs, Au_{15} NCs-DTPAA-Gd and Omnipaque. The in vitro fluorescence imaging was performed under UV light (365 nm) and Caliper IVIS Lumina II imaging system and Berthold LB983 live animal imaging system (Berthold Technologies, Germany, ex = 485 nm; em = 700 nm). The in vitro MR imaging of Au_{15} NCs-DTPAA-Gd and Magnevist was obtained using 3.0 T MR scanner with CUBE T_1 sequence: Freq. FOV, 10.0 mm^2; phase FOV, 1.00 mm^2; slice thickness, 1.0 mm; spacing, 0.2mm; TR, 400.0 ms; TE, 9 ms; matrix, 196 × 196; NEX, 3. The longitudinal (T_1) and transverse (T_2) relaxation times of Au_{15}NCs-DTPAA-Gd at different Gd^{3+} concentrations were determined using 3.0 T MR scanner (Discovery 750, General Electric Company, America) with the pulse sequence time parameters: Freq. FOV, 10.0 mm^2; phase FOV, 1.00 mm^2; echo time (TE), 160 ms; repetition time (TR), 600 ms; slice thickness, 1 mm; spacing, 1.0 mm. The linear fitting of inverse T_1 and T_2 relaxation time ($1/T_1$ and $1/T_2$) as a function of Gd concentration (mM) were taken to calculate the T_1 (r_1) and T_2 (r_2) relaxivity. The slope of the fitting line is the relaxivity.

Stability Analysis

The colloidal stability of the Au_{15}NCs-DTPAA-Gd was estimated by UV-visible-NIR UV1800 spectrophotometry, 960PC spectrofluorometer and 3.0 T MR scanner. Au_{15}NCs-DTPAA-Gd nanohybrids were incubated in phosphate-buffered saline (PBS) for a period of time (0 d, 7 d, 15 d, 30 d) at room temperature. For MRI, the incubated Au_{15}NCs-DTPAA-Gd nanohybrids were precipitated by ethanol via centrifugation several cycles to remove free Gd^{3+} and finally re-dispersed in the above solutions for MRI.

In vitro Cytotoxicity Studies

293T cells and HepG2 cells were planted into 96-well plates at a density of 1×10^4 cells. For MTT assay, cells in logarithmic growth were incubated with various concentrations of Au_{15}NCs-DTPAA-Gd for 24 h, and the cells treated with PBS as control. Thereafter, 20 μL of MTT solution (5 mg/mL) was added into each well and incubated for 4 h at 37°C, followed by removal of the medium and addition of 200 μL DMSO to dissolve the formed purple formazan crystals. Next, the plates were shaken for 15 min. The absorbance (OD) at 490 nm was recorded by microplate reader (Thermo Scientific, USA) to measure

the proliferative capacity of each group. Five wells of each concentration were set up to obtain the average value. The relative viability ratios of treated groups were calculated by the percentage of OD_{490} value of the treated cells over the untreated cells.

Cell Uptake

Intracellular uptake of Au_{15}NCs-DTPAA-Gd was measured in HepG2 cells and 293T cells. Cells were grown on 14 mm glass coverslips and allowed to adhere for 24 h. After co-incubation with 10 mg/mL Au_{15}NCs-DTPAA-Gd for different times, the cells were washed with PBS sufficiently to remove excess nanoclusters and fixed with 4% paraformaldehyde, and nuclei of the cells were stained with 4′-6-diamidino-2-phenylindole (DAPI, 1 mg/mL in PBS, invitrogen). DAPI emission was recorded between 440 and 470 nm, Au_{15} NCs-DTPAA-Gd emission images were obtained using a 630 nm longpass filter. Confocal fluorescence imaging studies were performed with confocal laser scanning microscope (Olympus FV10i, Tokyo, Japan).

In vivo CT/NIRF/MR Imaging

All animal experiments were carefully handled under the guidelines approved and supervised by the ethics committee of Institute of Radiation Medicine, Chinese Academy of Medical Sciences (Approval No.: IRM-DWLL-2019055). For CT imaging, a PBS solution of Au_{15}NCs-DTPAA-Gd (0.1 mol/L Au, 100 μL) was intravenously injected into BALB/c mice. The mice were placed in the LightSpeed VCT system and scanned at an interval of 5 mins under 120 kV, 80 mA with the slice thickness was 0.625 mm. For NIRF imaging, the nude mice were intravenously injected with Au_{15}NCs-DTPAA-Gd nanohybrids (0.1 mol/L Au, 100 μL). The fluorescence signals are collected by a Berthold LB983 live animal imaging system (λex = 485 nm/λem = 700 nm) at different time intervals. The T_1-weighted MR imaging for mice was performed by 3.0 T MR scanner before and after the injection of Au_{15}NCs-DTPAA-Gd nanohybrids solution (at a dosage of 0.1 mmol Gd/kg, 100 μL). T_1 FSE sequence was applied with the parameters: TR, 800 ms; TE, Min Full; slice thickness = 1.0 mm, spacing = 0.2 mm, matrix = 256 × 256. All experiments were repeated three times.

In vivo Pharmacokinetics and Biodistribution Analysis

For pharmacokinetic study, BALB/c mice were administered 150 μL of Au_{15}NCs-DTPAA-Gd via tail vein. Blood samples were collected from eye socket at indicated time points (5 min, 10 min, 15 min, 20 min, 30 min, 1 h, 2 h, 4 h, 6 h), followed by weighing and dissolution in digestive chloroazotic acid (V_{HCl}/V_{HNO3} = 1/3) to quantify the amount of Au and Gd via ICP-MS. Two-compartment pharmacokinetic model analysis of the data was performed with originpro software, and the pharmacokinetic parameters (e.g. elimination half-life, $T_{1/2}$) were calculated from the Gd contents in blood.

For biodistribution analysis, mice were sacrificed after 10 mins, 30 mins, 2 hrs and 24 hrs post-injection, and major organs (heart, liver, spleen, lung, kidney) were extracted and digested in aqua regia (6 mL) overnight. Solutions were then diluted to 10 mL with deionized water. Finally, Au and Gd contents in each organ were analyzed by ICP-MS. Results were expressed as the percentage of the injected dose g^{-1} (%ID/g). All experiments were repeated three times.

In vivo Biocompatibility Evaluation

Biocompatibility of Au_{15}NCs-DTPAA-Gd in vivo was evaluated by tissue Hematoxylin and eosin (H&E) staining. At 24 h and 2 weeks after injection with Au_{15}NCs-DTPAA-Gd, the mice were sacrificed under anesthetic conditions. Tissues of interest (heart, liver, spleen, lung, and kidney) were excised and preserved in a 10% formalin solution for 2 weeks. Then, the formalin fixed tissues from each organ were embedded into paraffin and sectioned into 4 mm thickness. Each histological section was documented by a dissecting microscope. The tissues were sectioned into 4-mm thickness. Each histological section was documented by a dissecting microscope. The histological assessment was done with the help of the pathologist. Six mice injected with Au_{15}NCs-DTPAA-Gd served as experimental group. We chose three tissue slices from each organ to perform H&E staining experiments.

Results and Discussion

Synthesis and Characterization of Au_{15} NCs-DTPAA-Gd

In our study, the Au_{15}NCs were synthesized by a one-step reduction method according to our previous optimized protocol.[26] Fifteen gold atoms form stable Au_{15}NCs with glutathione via a strong thiolate-Au interaction. Au_{15}NCs-DTPAA-Gd were synthesized via a classical amide reaction (Scheme 1). As determined by TEM (Figure 1A), the monodispersed spherical Au_{15}NCs have a mean diameter of less than 1.0 nm. After conjugation with DTPAA-Gd,

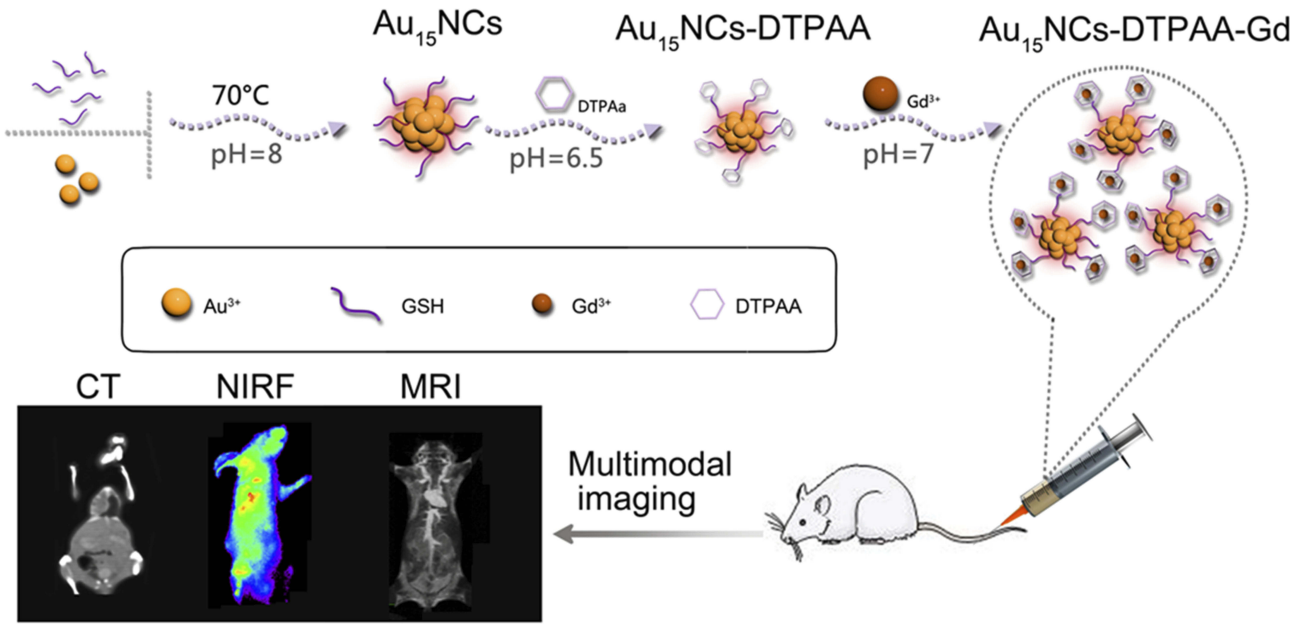

Scheme 1 Schematic illustration of the synthetic procedure and multimodal imaging for Au_{15}NCs-DTPAA-Gd nanohybrids.

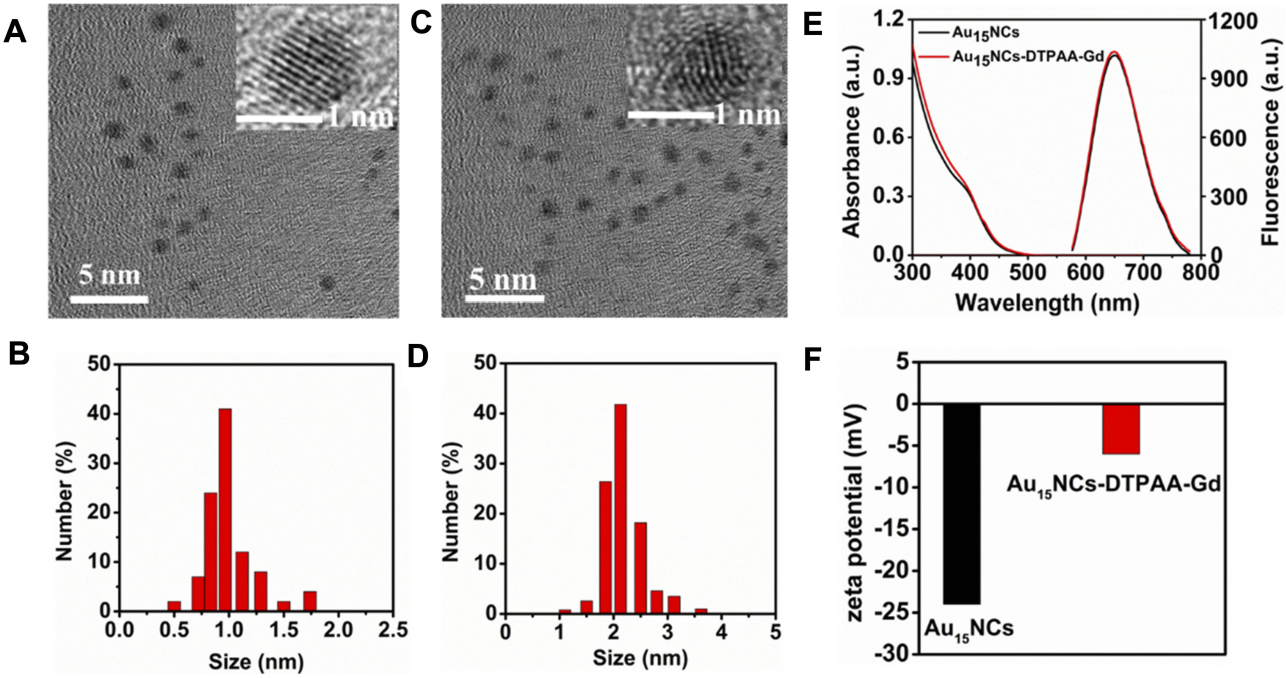

Figure 1 Characterization of the nanohybrids. TEM images of (**A**) Au_{15}NCs and (**C**) Au_{15}NCs-DTPAA-Gd; Size distribution histograms of (**B**) Au_{15}NCs and (**D**) Au_{15}NCs-DTPAA-Gd; (**E**) UV-visible-NIR absorbance spectra and fluorescence emission spectra of Au_{15}NCs and Au_{15}NCs-DTPAA-Gd in PBS. (**F**) Zeta potentials of Au_{15}NCs and Au_{15}NCs-DTPAA-Gd.

the well-dispersed Au_{15}NCs-DTPAA-Gd nanohybrids remain a spherical shape and an average size of approximately 1.0 ± 0.4 nm with no significant change, as shown in Figure 1B. Elemental analysis by the corresponding EDS spectrum confirmed the composition and atomic distribution of the synthetic nanohybrids. The spectra and mapping of Au_{15}NCs-DTPAA-Gd exhibit the presence of Au, Gd, C, and O (Figure S1), with different colors consistent with the chemical composition in the Au_{15}NCs-DTPAA-Gd nanohybrids. ICP-MS results show that the ratio between Gd and Au of Au_{15}NCs-DTPAA-Gd is about 1 to 1, which confirms that about fifteen Gd-DTPAA can conjugate with glutathione

from the surface of the Au cluster via an amide bond. Due to further increasing the Gd^{3+} relative to the Au_{15}NCs, the MRI capability of the synthesized Au_{15}NCs-DTPAA-Gd is not significantly improved, so we chose this ratio. For better application in vivo, the hydrodynamic diameter of Au_{15}Ns and Au_{15}NCs-DTPAA-Gd nanohybrids was measured by dynamic light scattering (DLS). The hydrodynamic diameter of Au_{15}NCs is 1.0 ± 0.3 nm (Figure 1B) and that of Au_{15} NCs-DTPAA-Gd is 2.5 ± 0.4 nm (Figure 1C). The hydrodynamic diameter is slightly larger than that observed with TEM, which results from the hydration of rGSH and DTPAA-Gd in water. Figure 1E displays the UV-visible-NIR absorption spectra and emission spectra of Au_{15}NCs and Au_{15}NCs-DTPAA-Gd. A typical absorption spectrum of Au_{15}NCs with distinct peaks at 370/410 nm is plotted in black solid line which is consistent with the reported literature.[27] Unlike the most popular and well-known spherical, large gold nanoparticles (AuNPs), AuNCs do not exhibit surface plasmon resonance (SPR) absorption in the visible region.[16,28,29] It is apparent that the absorption band of Au_{15} NCs-DTPAA-Gd is similar to that of Au_{15}NCs. It can be speculated that the introduction of DTPAA-Gd has no obvious effect on the Au_{15}NCs, and no AuNPs are formed to stimulate surface plasmon resonance under these conditions. By fluorescence spectrophotometry, the emission spectra of Au_{15}NCs-DTPAA-Gd and Au_{15}NCs are similar with range of 550–800 nm peaking at 680 nm, suggesting their deep tissue penetration ability. The quantum yields of Au_{15} NCs and Au_{15}NCs-DTPAA-Gd were measured to be 7.8% and 7.6% at λ_{ex} 470 nm, respectively.[15,29,30] The zeta potentials of Au_{15}NCs and Au_{15}NCs-DTPAA-Gd are about −5 mV and −24 mV, respectively (Figure 1F). The carboxylic groups of rGSH and DTPAA on the surface of the Au_{15}NCs may cause Au_{15}NCs and Au_{15}NCs-DTPAA-Gd to be negatively charged. These results indicate Gd functionalization of Au_{15} NCs by amide reaction is feasible.

In vitro CT/NIRF/MR Imaging

The synthesized Au_{15}NCs-DTPAA-Gd possess excellent three model imaging properties. Owing to the higher atomic numbers and electron densities (79, 19.32 g/cm^3) of gold element than that of iodine (53, 4.93 g/cm^3), the attenuation intensity of Au_{15}NCs-DTPAA-Gd was thus measured to assess the feasibility of their application as CT contrast agent. The CT images of Au_{15}NCs-DTPAA-Gd nanohybrids at various concentration levels in Figure 2A indicate an obvious increase of the brightness with the increase of the hybrid concentration. Quantitative calculation (Figure 2B) confirms a linear relationship between the attenuation intensity and the content of Au in the nanohybrids. What is particularly remarkable is that there is almost twofold amplified attenuation intensity of Au_{15}NCs-DTPAA-Gd compared with Omnipaque at equivalent concentration (I or Au). It is additionally demonstrated that the attenuation intensity of Au_{15}NCs-DTPAA-Gd is higher than that of Au_{15} NCs at the same Au concentrations. The phenomenon may be attributed to the existence of Gd ions possessing the relatively high atomic number and electron densities (64, 7.895 g/cm^3),[31] which results in synergistic enhancement of CT imaging capability. These observations well illustrate that the prepared Au_{15}NCs-DTPAA-Gd provide a promising contrast agent for CT imaging.

The photographs in Figure 3A and B display that the brown solution of Au_{15}NCs and Au_{15}NCs-DTPAA-Gd (room light) emitted similar intense-red fluorescence under UV light (365 nm). As NIRF imaging agents, Au_{15}NCs show strong quantum confinement effects and molecule-like properties while avoiding the photobleaching problems of conventional organic dyes. As shown in Figure 3C, both Au_{15}NCs

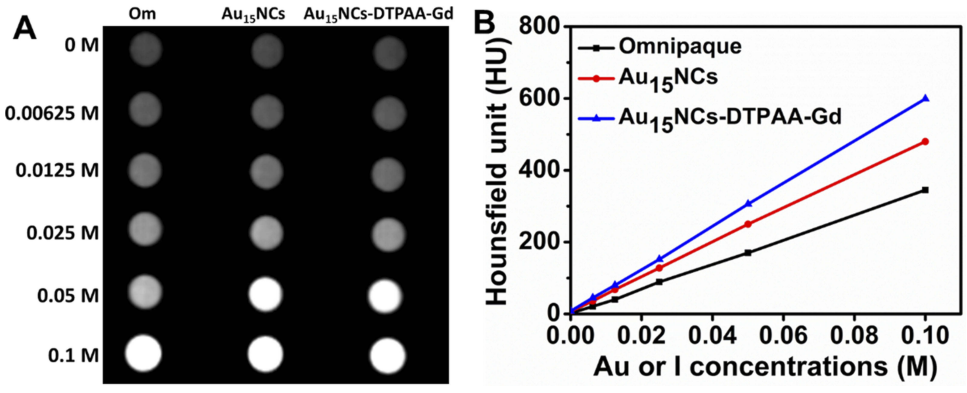

Figure 2 (**A**) In vitro CT imaging of Omnipaque, Au_{15}NCs and Au_{15}NCs-DTPAA-Gd. (**B**) The corresponding X-ray attenuation intensity plot at various concentrations (0, 0.00625, 0.0125, 0.025, 0.05 and 0.1 mol L^{-1}).

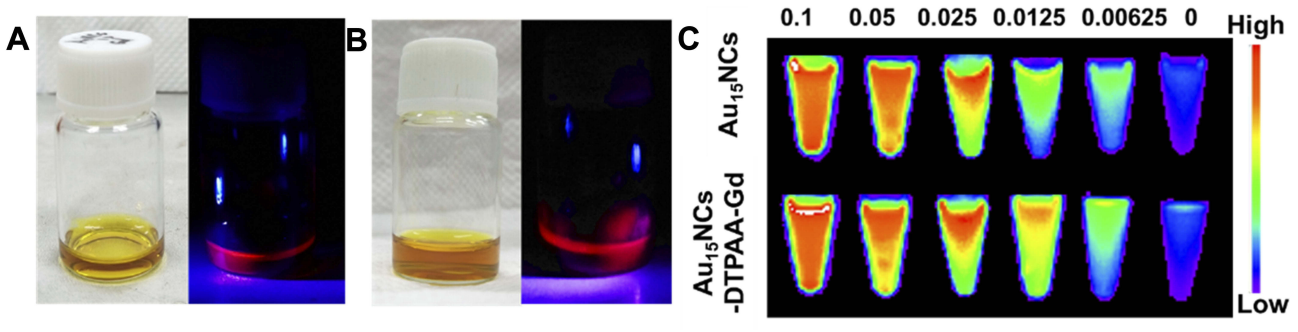

Figure 3 Photographs of (**A**) Au_{15}NCs and (**B**) Au_{15}NCs-DTPAA-Gd under irradiation by natural light (left) and UV light (365 nm, right). (**C**) In vitro NIFR imaging of Au_{15} NCs and Au_{15}NCs-DTPAA-Gd with different concentrations.

and Au_{15}NCs-DTPAA-Gd nanohybrids exhibit similarly obvious enhancement of the NIRF signal with an increase of Au concentration. Moreover, the introduction of an additional functional DTPAA-Gd makes no effect on fluorescence property of Au_{15}NCs. DTPAA is directly connected to glutathione on the surface of Au_{15}NCs via an amide bond, which does not cause glutathione to detach significantly from the surface of gold. Therefore, the surface function of Au_{15}NCs is not affected greatly. Meanwhile, the introduction of DTPAA-Gd did not significantly increase the size of Au_{15}NCs. These factors may lead to no significant change in the fluorescence of Au_{15}NCs-DTPAA-Gd compared with that of Au_{15}NCs.

It is known that Gd^{3+} is able to induce the longitudinal relaxation of water protons, shorten the longitudinal relaxation time (T_1) and enhance MR imaging effect.[32] In the present case, T_1 and T_2 values of Au_{15}NCs-DTPAA-Gd nanohybrids at various concentrations in aqueous medium were measured to estimate the longitudinal (r_1) and transverse (r_2) relaxivity. A dose-dependent brightening effect is observed in T_1-weighted MR imaging (Figure 4A), r_1 and r_2 were calculated to be 8.5 and 9.6 mM^{-1} s^{-1} (with an r_2/r_1 ratio of 1.13) (Figure 4C), respectively. Importantly, MR signal intensity of Au_{15}NCs-DTPAA-Gd is much stronger than that of Magnevist (Figure 4A and B), and the r_1 of Au_{15}NCs-DTPAA-Gd exhibits about two times than that of Magnevist (3.97 mM^{-1} S^{-1}). Due to fifteen Gd-chelates formed on the surface of Au_{15}NCs, it may be speculated that possible explanations for relatively higher r_1 value and MR signal of Au_{15} NCs-DTPAA-Gd compared to Magnevist include: (i) an increase in rotational correlation time by virtue of the attachment of the metal chelate to macromolecules, (ii) an increase in the number of outer sphere-coordinated water molecules entrapped by the Au_{15}NCs@GSH, and (iii) the cooperative induction effect by the surface gadolinium in Au_{15}NCs-DTPAA-Gd.[33,34] This indicates a promising potential for utilizing Au_{15}NCs-DTPAA-Gd nanohybrids as a superior T_1-weighted MR imaging contrast agent.

Stability Analysis and Cytotoxicity

For further biomedical applications of Au_{15}NCs-DTPAA-Gd, it is necessary to check stability in bio-fluids. The colloidal stability of Au_{15}NCs-DTPAA-Gd dissolved in PBS was monitored constantly at different storage time points. In vitro MRI Au_{15}NCs-DTPAA-Gd (Figure 5A) shows no significant

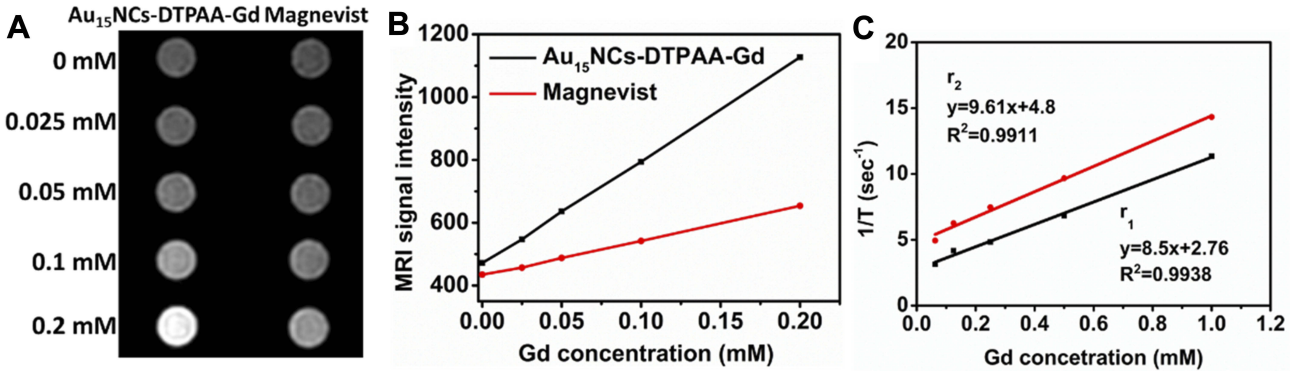

Figure 4 (**A**) In vitro T_1-weighted MR images of Magnevist and Au_{15}NCs-DTPAA-Gd. (**B**) The corresponding MR signal intensity. (**C**) T_1 and T_2 relaxivity plots as a function of Gd concentration (0, 0.025, 0.05, 0.1 and 0.2 mmol L^{-1}), the corresponding slopes give rise to r_1 and r_2 values of Au_{15}NCs-DTPAA-Gd.

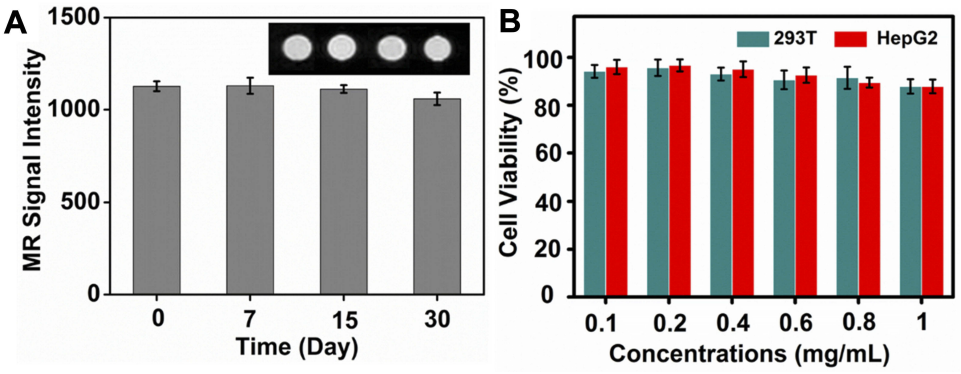

Figure 5 (**A**) The MR images and signal intensity of Au_{15}NCs-DTPAA-Gd incubated in PBS for different time (0 d, 7 d, 15 d, 30 d) at room temperature. The data is represented as mean ± standard deviation, n=3/group. (**B**) Viabilities of 293T and HepG2 cells treated with different concentrations of Au_{15}NCs-DTPAA-Gd nanohybrids for 24 h.

decrease in MRI signals over time, which confirms that the chelated Gd^{3+} of Au_{15}NCs-DTPAA-Gd is excellently stable. Figure S2 shows that no significant changes in the absorption peak position or fluorescence intense happened at different time points. Over this period, there is no precipitation in the solution, and the color of the solution does not change significantly (Figure S2 inset), which demonstrates favorable water dispersibility of Au_{15}NCs-DTPAA-Gd nanohybrids. These results confirm that the physicochemical properties of Au_{15} NCs in Au_{15}NCs-DTPAA-Gd nanohybrids are quite stable.

The in vitro cytotoxicity of Au_{15}NCs-DTPAA-Gd against 293T and HepG2 cells was investigated via MTT assays. As shown in Figure 5B, more than 90% of the 293T and HepG2 cells all stay alive even when the concentration of Au_{15}NCs-DTPAA-Gd reaches up to 1 mg/mL concentration. This clearly demonstrates that Au_{15}NCs-DTPAA-Gd possess a favorable biocompatibility.

Cell Uptake Studies

In this work, we want to initially explore the potential of Au_{15}NCs-DTPAA-Gd as multimodal imaging probe of tumors, so the affinity of Au_{15}NCs-DTPAA-Gd to tumor cells is of vital significance. The in vitro intake of Au_{15} NCs-DTPAA-Gd by HepG2 and 293T cells was monitored with confocal fluorescence microscopy. As illustrated in Figure 6, when HepG2 cells were incubated with Au_{15}

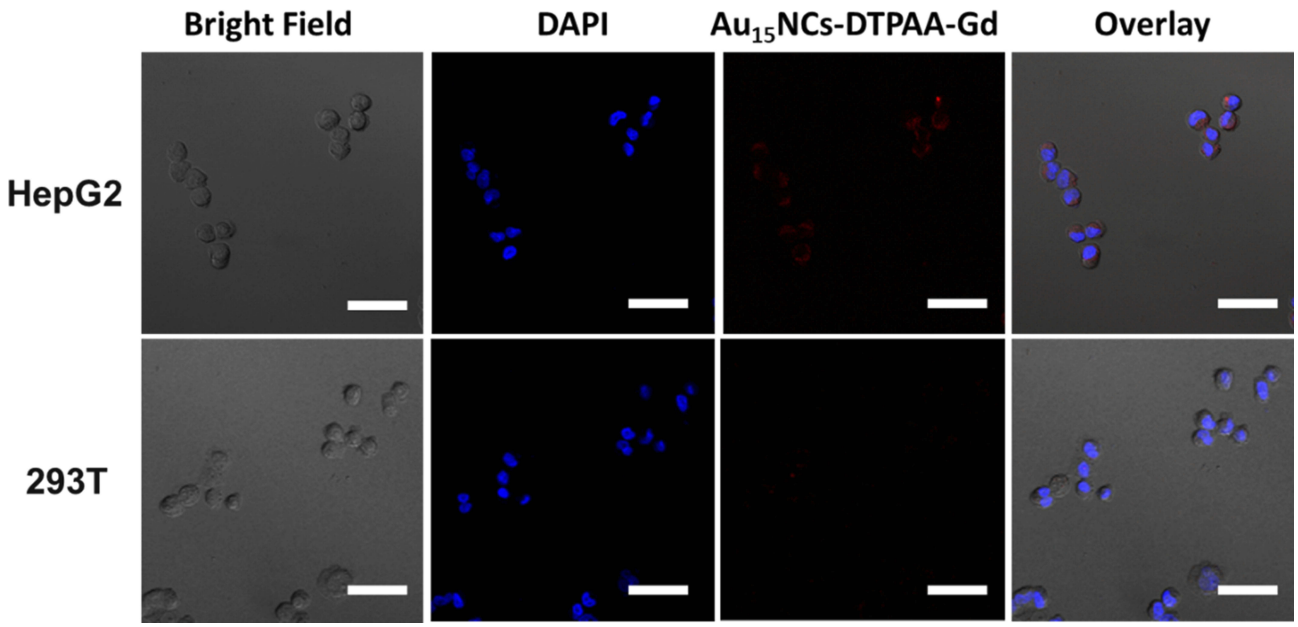

Figure 6 The Confocal microscopy images of HepG2 and 293T cells incubated for 24 h with Au_{15}NCs-DTPAA-Gd nanohybrids. Scale bar: 50 μm.

NCs-DTPAA-Gd for 24 h, obvious-red fluorescence was observed and mainly existed around the nucleus at 405 nm excitation. Compared with HepG2 cells, 293T cells incubated with Au_{15}NCs-DTPAA-Gd for 24 h did not exhibit significant fluorescence. These results illustrated Au_{15} NCs-DTPAA-Gd may efficiently enter cytoplasm through endocytosis of active cancer cells.

In vivo CT/NIRF/MR Imaging

The feasibility of Au_{15}NCs-DTPAA-Gd as in vivo CT/NIRF/MR trimodal imaging agent was exploited on BALB/c mice. Firstly, the accumulation of Au_{15}NCs-DTPAA-Gd in liver makes this region brighter in CT image after 5-min injection with respect to that observed without administration (Figure 7Aa). The X-ray attenuation intensities in the liver

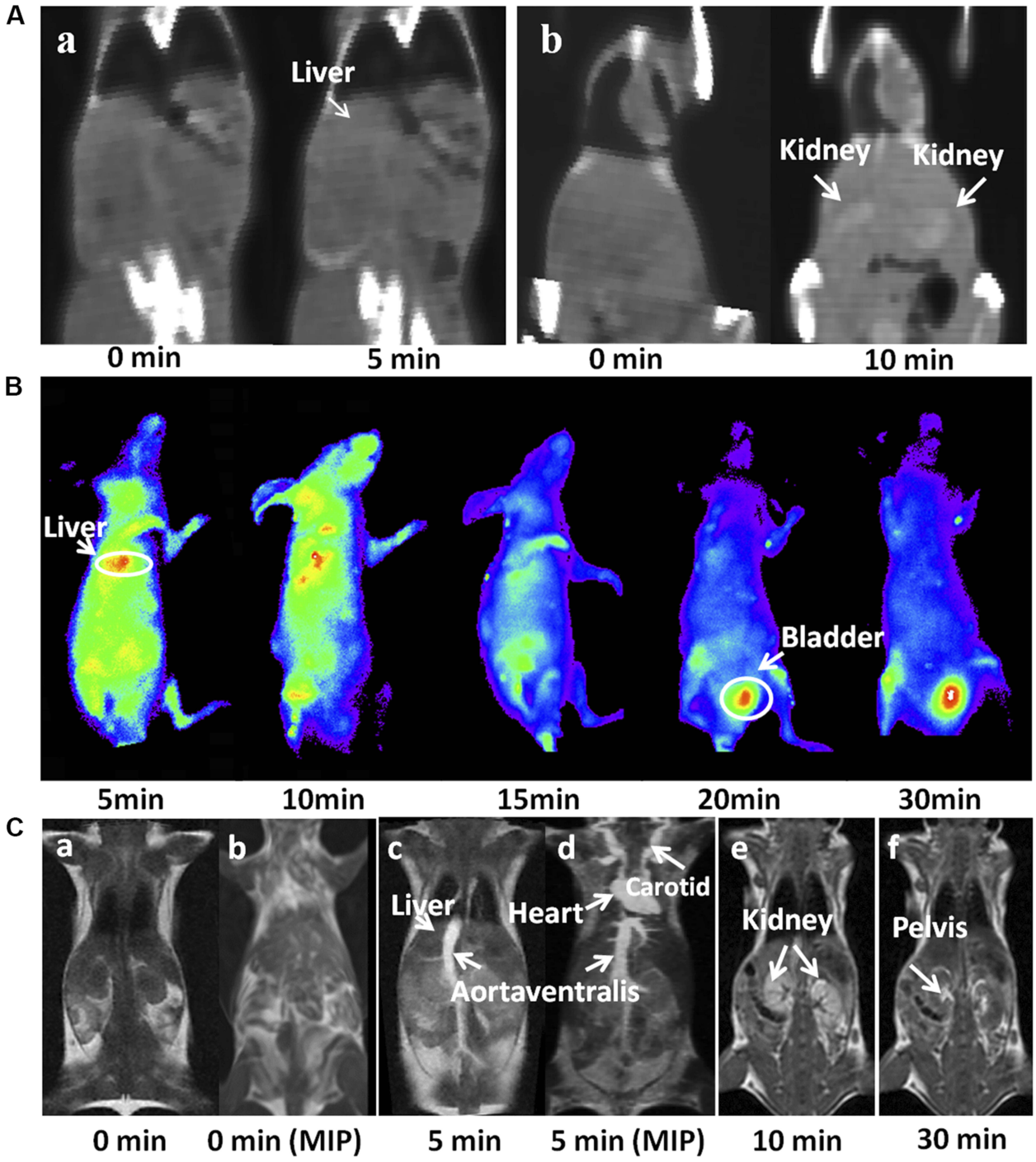

Figure 7 In vivo (**A**) CT, (**B**) NIRF, and (**C**) T_1-weighted MR imagingat different time intervals after intravenous injection of Au_{15}NCs-DTPAA-Gd. CT imaging of the liver (**A**a) and kidneys (**A**b) before and after injection. T1-weighted MR (**C**a) and Maximum Intensity Projection (MIP) imaging (**C**b) before injection. T1-weighted MR (**C**c) and MIP (**C**d) imaging of cardiovascular after 5-min injection. T1-weighted MR imaging after 10-min and 30-min injection (**C**e-f).

region before and after Au_{15}NCs-DTPAA-Gd administration were quantitatively calculated to be 64.7 ± 2.2 HU and 120.5 ± 3.4 HU, respectively. After 10-min injection, both kidneys become clearer and brighter than those observed without administration (Figure 7Ab). In the following, NIRF imaging was performed by intravenous administration of Au_{15}NCs-DTPAA-Gd. Figure 7B illustrates an obvious enhancement on the fluorescence signal in mice liver after a 5-min injection. It is seen that obvious signal is observed in bladder at 20-min post-injection, indicating that Au_{15}NCs-DTPAA-Gd is mainly eliminated via urinary route. Subsequently, T_1-weighted MR images of mice were acquired before and after administering medication. It is seen that the liver is brightened after a 5-min injection (Figure 7Cc). In addition, T_1-weighted MRI and MIP images of cardiovascular (Figure 7Cc-d) after a 5-min injection were acquired. It is clearly observed that the cardiovascular function of the mice was significantly enhanced after injection. As shown in Figure 7Ce, both kidneys are brightened after 10-min injection, which are consistent with that observed in CT. Figure 7Cf shows that the bilateral renal pelvis is clear after 30-min injection. These observations suggest that the present Au_{15}NCs-DTPAA-Gd platform exhibits favorable CT/NIRF/MR imaging capability in vivo.

In vivo Pharmacokinetics and Biodistribution Analysis

To explore the pharmacokinetic and biodistribution of Au_{15}NCs-DTPAA-Gd, element gold and Gd of blood and organs were proceeded after injection of Au_{15}NCs-DTPAA-Gd. As seen in Figure S3A, blood circulation behavior of Au_{15}NCs-DTPAA-Gd is excellently conformed to two-compartment pharmacokinetics with blood elimination half-life ($T_{1/2}$) of 24.9 ± 0.5 min. The ideally longer elimination half-life compared to Omnipaque and Magnevist might aid to imaging and minimizing organ damage. The biodistribution of Au_{15}NCs-DTPAA-Gd based on ICP-MS (Figure S3B) reveals that the elemental distribution of Au in the different organs is similar to that of Gd^{3+} ions in the mice post-injection of Au_{15}NCs-DTPAA-Gd, further suggesting that Au_{15}NCs-DTPAA-Gd are formed by the assimilation of Au_{15}NCs with Gd^{3+} ions rather than as a result of a mixture of Au_{15}NCs and Gd^{3+} ions. The ICP-MS results also indicate a fast urine elimination of Au_{15}NCs-DTPAA-Gd, as the Au_{15}NCs-DTPAA-Gd significantly accumulate in the kidney post-injection and are almost cleared from the kidney with a prolonged circulation time of 2 hrs. Moreover, a small amount of Au and Gd remain in heart, liver, spleen, and lung post-injection, suggesting a low uptake of Au_{15}NCs-DTPAA-Gd by Reticulo-Endothelial System (RES) tissues and that Au_{15}NCs-DTPAA-Gd are not significantly retained in the lung. These observations indicate that Au_{15}NCs-DTPAA-Gd are safe for in vivo biomedical imaging applications.

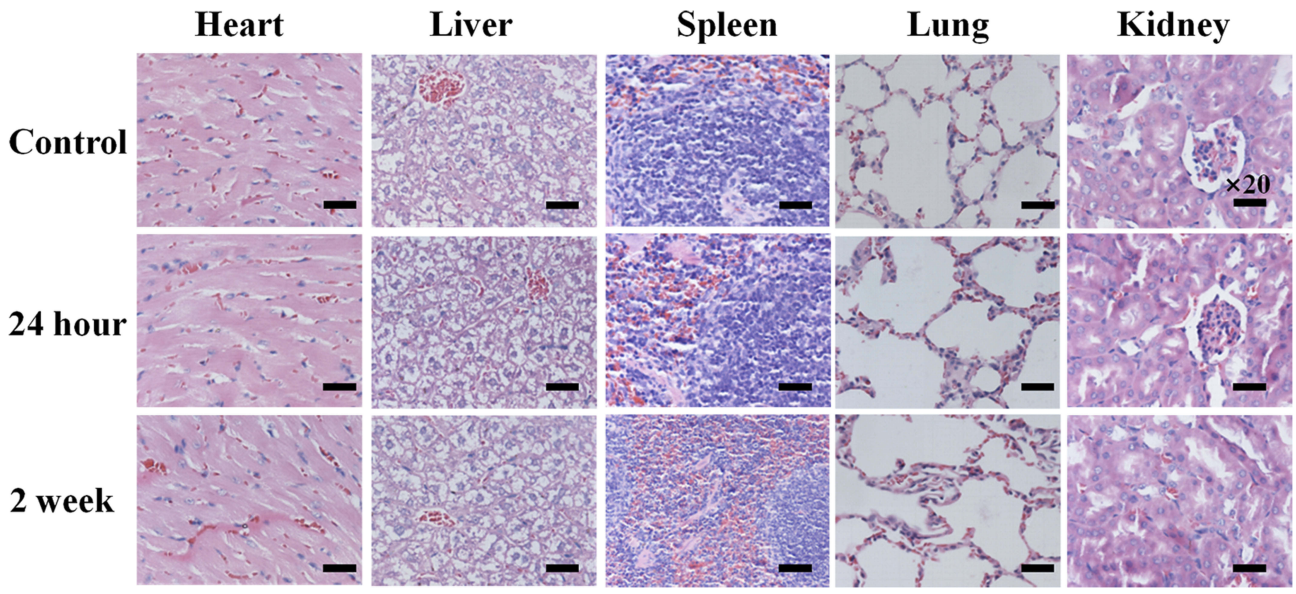

Figure 8 In vivo biocompatibility evaluation of Au_{15}NCs-DTPAA-Gd. Histological analyses of main organs (heart, liver, spleen, lung and kidney) stained with hematoxylin and eosin (H&E) from the mice injected with Au_{15}NCs-DTPAA-Gd.

In vivo Biocompatibility Evaluation

The in vivo toxicity of Au_{15}NCs-DTPAA-Gd was evaluated by monitoring the pathological changes of several major organs of all mice using H&E staining sections. As shown in Figure 8, compared to the control mice treated with PBS, the injection of the Au_{15}NCs-DTPAA-Gd seems not to induce any noticeable changes in the morphology and other lesions (such as necrosis and inflammatory) of the organ sections from all mice. These results imply that Au_{15}NCs-DTPAA-Gd possess good biocompatibility for applications.

Conclusions

In this work, a facile approach is developed for the configuration of multimodal imaging synergistical imaging nanohybrids (Au_{15}NCs-DTPAA-Gd). Compared with conventional multimodal nanoplatform usually requiring a complicated synthetic procedure, Au_{15}NCs-DTPAA-Gd nanohybrids have the potential to overcome the limitations of interference between imaging elements. The nanohybrids are highly water-dispersible, biocompatible and stable, which can not only realize CT/MRI collaborative imaging, but also exhibit photoluminescent capability in NIR region. Under the condition of meeting the needs of diagnosis, the Au_{15}NCs-DTPAA-Gd with a lower dose than traditional contrast agents can reduce the toxicity of contrast agents as much as possible. Overall, the developed Au_{15}NCs-DTPAA-Gd nanoplatform provides an efficient candidate as an imaging contrast agent for disease diagnosis, especially for early accurate detection of tumors.

Acknowledgments

This work was financially supported by Key Program of the Tianjin Health and Family Planning Commission (16KG115). All the financial supports are gratefully acknowledged.

Disclosure

The authors report no conflicts of interest in this work.

References

1. Louie A. Multimodality imaging probes: design and challenges. *Chem Rev*. 2010;110:3146–3195. doi:10.1021/cr9003538
2. Lee DE, Koo H, Sun IC, Ryu JH, Kim K, Kwon IC. Multifunctional nanoparticles for multimodal imaging and theragnosis. *Chem Soc Rev*. 2012;41:2656–2672. doi:10.1039/C2CS15261D
3. Liu J, Zheng X, Yan L, et al. Bismuth sulfide nanorods as a precision nanomedicine for in vivo multimodal imaging-guided photothermal therapy of tumor. *ACS Nano*. 2015;9:696–707. doi:10.1021/nn506137n
4. Hu Y, Zhou Y, Zhao N, Liu F, Xu F-J. Multifunctional pDNA-conjugated polycationic Au nanorod-coated Fe3O4 hierarchical nanocomposites for trimodal imaging and combined photothermal/gene therapy. *Small*. 2016;12:2459–2468. doi:10.1002/smll.201600271
5. Liu Y, Ai K, Lu L. Nanoparticulate X-ray computed tomography contrast agents: from design validation to in vivo applications. *Acc Chem Res*. 2012;45:1817–1827. doi:10.1021/ar300150c
6. Marradi M, Chiodo F, Garcia I, Penades S. Glyconanoparticles as multifunctional and multimodal carbohydrate systems. *Chem Soc Rev*. 2013;42:4728–4745. doi:10.1039/c2cs35420a
7. Hemmer P. Toward molecular-scale MRI. *Science*. 2013;339:529–530. doi:10.1126/science.1233222
8. Wood CS, Stevens MM. Improving the image of nanoparticles. *Nature*. 2016;539:505–506. doi:10.1038/nature20478
9. Zhao F, Li X, Li J, et al. Activatable ultrasmall gold nanorods for "off–on" fluorescence imaging-guided photothermal therapy. *J Mater Chem B*. 2017;5:2145–2151. doi:10.1039/C6TB02873J
10. Kim S, Lim YT, Soltesz EG, et al. Near-infrared fluorescent type II quantum dots for sentinel lymph node mapping. *Nat Biotechnol*. 2004;22:93–97. doi:10.1038/nbt920
11. Yang Y, Wang S, Xu C, Xie A, Shen Y, Zhu M. Improved fluorescence imaging and synergistic anticancer phototherapy of hydrosoluble gold nanoclusters assisted by a novel two-level mesoporous canal structured silica nanocarrier. *Chem Commun*. 2018;54:2731. doi:10.1039/C8CC00685G
12. Liu X, Liu L, Hu X, et al. Multimodal bioimaging based on gold nanorod and carbon dot nanohybrids as a novel tool for atherosclerosis detection. *Nano Res*. 2018;11:1262–1273. doi:10.1007/s12274-017-1739-4
13. Han L, Xia JM, Hai X, Shu Y, Chen XW, Wang JH. Protein-stabilized gadolinium oxide-gold nanoclusters hybrid for multimodal imaging and drug delivery. *ACS Appl Mater Interfaces*. 2017;9:6941–6949. doi:10.1021/acsami.7b00246
14. Sun Y, Zhu X, Peng J, Li F. Core–shell lanthanide upconversion nanophosphors as four-modal probes for tumor angiogenesis imaging. *ACS Nano*. 2013;7:11290–11300. doi:10.1021/nn405082y
15. Li Z, Peng H, Liu J, et al. Plant protein-directed synthesis of luminescent gold nanocluster hybrids for tumor imaging. *ACS Appl Mater Interfaces*. 2018;10:83–90. doi:10.1021/acsami.7b13088
16. Jin R. Quantum sized, thiolate-protected gold nanoclusters. *Nanoscale*. 2010;2:343–362. doi:10.1039/B9NR00160C
17. Whetten RL, Khoury JT, Alvarez MM, et al. Nanocrystal gold molecules. *Adv Mater*. 1996;8:428–433. doi:10.1002/(ISSN)1521-4095
18. Zheng Y, Lai L, Liu W, Jiang H, Wang X. Recent advances in biomedical applications of fluorescent gold nanoclusters. *Adv Colloid Interface Sci*. 2017;242:1–16. doi:10.1016/j.cis.2017.02.005
19. Jadzinsky PD, Calero G, Ackerson CJ, Bushnell DA, Kornberg RD. Structure of a thiol monolayer-protected gold nanoparticle at 1.1 a resolution. *Science*. 2007;318:430–433. doi:10.1126/science.1148624
20. Luo Z, Yuan X, Yu Y, et al. From aggregation-induced emission of Au(I)–thiolate complexes to ultrabright Au(0)@Au(I)–thiolate core–shell nanoclusters. *J Am Chem Soc*. 2012;134:16662. doi:10.1021/ja306199p
21. Gu W, Zhang Q, Zhang T, et al. Hybrid polymeric nano-capsules loaded with gold nanoclusters and indocyanine green for dual-modal imaging and photothermal therapy. *J Mater Chem B*. 2016;4:910–919. doi:10.1039/C5TB01619C
22. Wang C, Yao Y, Song Q. Gold nanoclusters decorated with magnetic iron oxide nanoparticles for potential multimodal optical/magnetic resonance imaging. *Mater Chem C*. 2015;3:5910–5917. doi:10.1039/C5TC00290G
23. Connor EE, Mwamuka JN, Gole A, Murphy CJ, Wyatt MD. Gold nanoparticles are taken up by human cells but do not cause acute cytotoxicity. *Small*. 2005;1:325–327. doi:10.1002/(ISSN)1613-6829
24. Popovtzer R, Agrawal A, Kotov NA, et al. Targeted gold nanoparticles enable molecular CT imaging of cancer. *Nano Lett*. 2008;8:4593–4596. doi:10.1021/nl8029114
25. Zhang Y, Wu M, Wu M, et al. Study of fluorescence and CT bimodal imaging of ultrasmall gold nanoclusters. *Acta Chim Sinica*. 2018;76:709–714. doi:10.6023/A18060225

26. Yu Y, Chen X, Yao Q, Yu Y, Yan N, Xie J. Scalable and precise synthesis of thiolated Au 10–12, Au 15, Au 18, and Au 25 nanoclusters via pH controlled CO reduction. *Chem Mater*. 2013;25:946. doi:10.1021/cm304098x
27. Negishi Y, Nobusada K, T T. Glutathione-protected gold clusters revisited: bridging the gap between gold(I)−thiolate complexes and thiolate-protected gold nanocrystals. *J Am Chem Soc*. 2005;127:5261–5270. doi:10.1021/ja042218h
28. Chen LY, Wang CW, Yuan Z, Chang HT. Fluorescent gold nanoclusters: recent advances in sensing and imaging. *Anal Chem*. 2015;87:216–229. doi:10.1021/ac503636j
29. QIAN H, ZHU M, WU Z, JIN R. Quantum sized gold nanoclusters with atomic precision. *Acc Chem Res*. 2012;45:1470–1479. doi:10.1021/ar200331z
30. Yuan X, Luo Z, Zhang Q, et al. Synthesis of highly fluorescent metal (Ag, Au, Pt, and Cu) nanoclusters by electrostatically induced reversible phase transfer. *ACS Nano*. 2011;5:8800–8808. doi:10.1021/nn202860s
31. Wang L, Xing H, Zhang S, et al. A Gd-doped Mg-Al-LDH/Au nanocomposite for CT/MR bimodal imagings and simultaneous drug delivery. *Biomaterials*. 2013;34:3390–3401. doi:10.1016/j.biomaterials.2013.01.070
32. Caravan P, Ellison JJ, Mcmurry TJ, Lauffer RB. Gadolinium(III) chelates as MRI contrast agents: structure, dynamics, and applications. *Chem Rev*. 1999;99:2293–2352. doi:10.1021/cr980440x
33. Park JY, Baek MJ, Choi ES, et al. Paramagnetic ultrasmall gadolinium oxide nanoparticles as advanced T 1 MRI contrast agent: account for large longitudinal relaxivity, optimal particle diameter, and in vivo T 1 MR images. *ACS Nano*. 2009;3:3663–3669. doi:10.1021/nn900761s
34. Aravindan L, Bicknell KA, Brooks G, Khutoryanskiy VV, Williams AC. Effect of acyl chain length on transfection efficiency and toxicity of polyethylenimine. *Int J Pharm*. 2009;378:201–210. doi:10.1016/j.ijpharm.2009.05.052